Application of femtosecond laser electronic excitation tagging (FLEET) velocimetry in a bladeless turbine

Jordan M. Fisher[1], James Braun[2], Terrence R. Meyer[1,2], and Guillermo Paniagua[1,2]

[1] School of Aeronautics and Astronautics, Purdue University, West Lafayette, IN, USA
[2] School of Mechanical Engineering, Purdue University, West Lafayette, IN, USA

E-mail: fishe193@purdue.edu (J Fisher), braun26@purdue.edu (J Braun), gpaniagua@purdue.edu (G Paniagua), and trmeyer@purdue.edu (T Meyer)

Received xxxxxx
Accepted for publication xxxxxx
Published xxxxxx

Abstract

Shock waves appear in numerous high-speed propulsion applications, including intakes, nozzles, and transonic and supersonic turbomachinery. The aerodynamic performance in bladeless turbines, which is designed for work extraction under such conditions, is dominated by flow separation induced by shock-wave pressure gradients. The large velocity gradients pose limitations on flowfield characterization using particle-based optical diagnostics, such as Particle Image Velocimetry (PIV) and Laser Doppler Anemometry (LDA). These limitations, along with challenges in seeding the flow, can be overcome by tracking the molecules already present in the flow. This paper presents kHz-rate femtosecond laser electronic excitation tagging (FLEET) to excite long-lived fluorescence of nitrogen molecules, acting as in-situ flow tracers. A multi-point variation of this approach was demonstrated in an optically accessible linear turbine test section, developed to investigate bladeless turbines. The femtosecond laser is coupled with an intensified CMOS camera with a frame rate of 200 kHz. High-speed measurements were made of the steady and unsteady performance in the bladeless turbine, with particular attention to capturing flow structures, spatial velocity gradients, and transient events such as unstarting of the supersonic passages.

Keywords: Molecular Tagging, Bladeless Turbine, Supersonic Velocity Measurements, Separated Flow, Shock-Boundary Layer Interaction, Velocimetry

1. Introduction

Bladeless axial turbines with a sinusoidal wavy surface enable power extraction from high-speed harsh environments (1,2), as sketched in Figure 1. Oblique shock waves cause a cyclic pressure differential across the wall geometry, which induces a torque on the rotating drum. To understand the complex flow physics occurring around the wavy hub geometry, which involves compression and separation shocks, experimental assessment of velocity field is required. A traditional measurement technique for obtaining spatio-temporally resolved velocity measurements is Particle Image Velocimetry (PIV). For the flow field in question, PIV may be compromised for several reasons. In the region of interest, several shock-boundary layer interaction patterns exist with consequent high spatial gradients in the velocity field. Due to non-negligible inertia, the particles used in PIV experience a finite relaxation time in response to changing velocity; and this

can cause a bias in measurement. Without diligent selection of the observation window and particle size, this effect will cause smearing of the flow features being interrogated (3,4). In simplified supersonic flows with low numbers of shocks this smearing can be accounted for (5); however, this becomes impractical in more complex experiments. Another challenge with PIV is obtaining near-wall data. PIV relies on laser light scattering from particles, and a by-product of this is laser scatter from solid boundaries in the test section. Wall scattering signal tends to be much brighter than particle scattering and the result of this is that data acquisition near walls and in boundary layers becomes increasingly difficult. To combat this, fluorescent PIV methods have been used (6). Seeding fluorescent particles into gas flows can, however, be hazardous to personal health and sensitive equipment. In large flow facilities, acquisition of large amounts of these particles also can become prohibitively expensive.

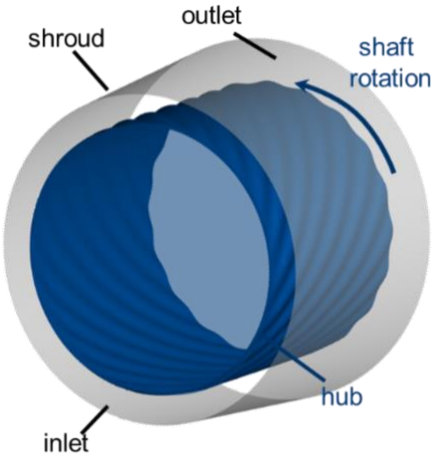

Figure 1. Three-dimensional view of a bladeless turbine.

PIV was initially attempted in bladeless turbine experiments. Consequently, laser scattering, particle density, and particle lag represented major challenges. To acquire velocity data in a simplified and more reliable manner, femtosecond laser electronic excitation tagging (FLEET) (7–9), a molecular tagging velocimetry (MTV) method which employs a femtosecond laser focused at a point to dissociate nitrogen molecules, was implemented. The recombination process of the excited state nitrogen produces a long-lived fluorescence signal, which can be sequentially imaged to measure velocity.

To perform FLEET, a femtosecond laser beam is focused to the point of interest in the flow field. Figure 2 sketches the FLEET application in a supersonic flow, and the subsequent imaging process. The focusing distance depends on the size and optical access of the experimental test section. An intensified camera is focused on the interrogation region. Once nitrogen molecules are excited by the laser, they emit visible broadband fluorescence, which can be observed for greater than 100 µs, depending on the flow conditions. With sequential imaging of the motion of the tagged molecules, velocity measurements can be made from the measured displacement and known time spacing between frames. Multiple images of the same excitation can be acquired, allowing for multiple streamwise velocity measurements. Adjustment of the camera magnification and time spacing between images can optimize the precision and dynamic range of the measurement technique, which is discussed in detail in (10). By increasing the image magnification, the spot displacement can occur over a larger number of pixels which leads to better resolution of the motion. By increasing the time delay between images, the signal can move farther which allows the uncertainty of the image centroid finding to occupy a lower percentage of the total displacement, thus increasing precision. However, increasing time delay has the added drawback of decreasing measurement spatial resolution since measurements are taken over a larger distance. An explanation of how these parameters were selected for this experiment is included in the optical equipment section.

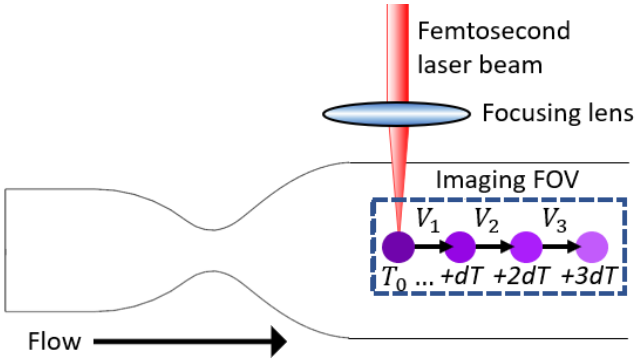

Figure 2. Schematic of generic FLEET experiment.

FLEET offers a wide range of applicability, and simplicity in the optical setup. Other molecular tagging techniques generally require molecules to be seeded into the flow (11,12) and/or careful alignment and overlap of multiple laser beams to produce and excite intermediate species (13,14). Alternatively, FLEET only requires one focused laser and one camera to perform measurements,

making it attractive for its ease of implementation. Although not always necessary, FLEET can be performed in a line-of-sight configuration only requiring one direction of optical access (15). Since the molecules being tagged are nitrogen, this method can be used in air or nitrogen flow facilities. Image acquisition for FLEET occurs with a time-delay from the initial excitation, and signals are emitted at a different wavelength. Therefore, laser scattering can be temporally and spectrally filtered, allowing for near-wall measurements to be collected. With proper camera sizing and timing, velocity dynamic range from tens to thousands of meters per second can be captured with uncertainties near one percent (16).

Recent advancements in FLEET have focused on evaluating the reliability of the measurement technique in more applied environments such as the 0.3-m Transonic Cryogenic Tunnel Facility at Nasa Langley (17). Much promise in gaining useful aerodynamic data such as wake profiles and pseudo-streamlines have been presented in this prior work with high accuracy and precision. Other researchers have presented progress on improving the temporal resolution via burst-mode FLEET up to the MHz rate to acquire rapid fluctuations in high speed flows (18). The present work reports on the use of kHz multi-point FLEET for characterizing the flow field and comparison with CFD model predictions in supersonic bladeless turbine environments. Specifically, this work utilizes this approach to resolve shock structures, steady and unsteady components of velocity, and transient behavior of the supersonic environment as it becomes unstarted. The multi-point variation is also evaluated for instantaneous shear stress measurements.

2. Experimental facilities

2.1. Wind tunnel facility

All experiments were performed in a linear blowdown wind tunnel at the Purdue Experimental Aero-thermal Laboratory (PETAL) (19). A 283 m^3 vacuum tank is present downstream of the test section to allow for high Mach and low Reynold's number operation. The system is drawn down to near vacuum before testing to allow the sonic throat to choke at lower total pressures. The facility was specially modified prior to this experiment to allow for supply of pure nitrogen at flow rates up to 6 kg/s. Flowing pure nitrogen has the effect of increasing signal quality and lifetime of FLEET measurements (8). The linear blowdown tunnel was designed to allow a high amount of access for optical diagnostics. For the tests reported in the current work, the tunnel was constructed with metal blanks on the top and back side, a large optical quartz window on the front, and the sonic throat/test section attached to the bottom. A schematic of the facility architecture is shown in Figure 3 (a).

2.2. Test section and operating conditions

Figure 3 (b) displays the arrangement of the supersonic test section. The wavy turbine shape is mounted in the lower part of the test section, downstream of a converging-diverging nozzle, in a region where the free-stream velocity exceeds Mach number 2. The wavy hub surface mimics a two-dimensional simplification of the three-dimensional bladeless turbine to enable detailed optical diagnostics with a variety of measurement techniques. For these tests, the mass flow was ~2 kg/s with a flow total temperature of 270 K. The Reynolds number based on the momentum thickness upstream of the wavy hub geometry was 91,000. The vacuum pressure at the onset of testing was 0.1 bar.

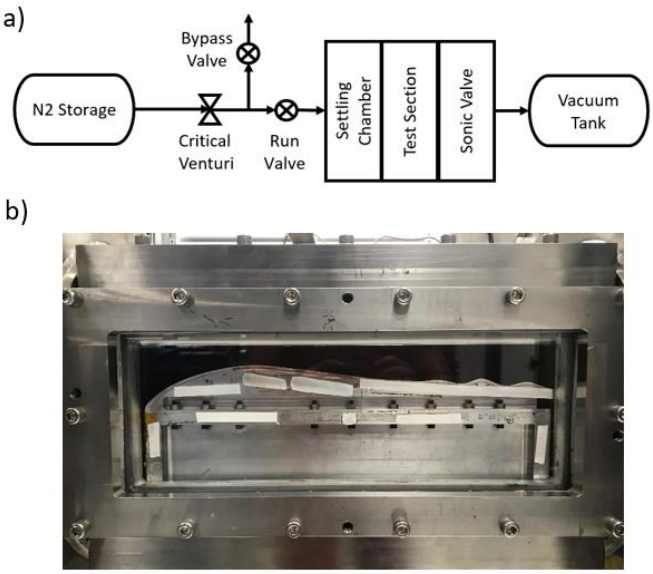

Figure 3. (a) Schematic of PETAL linear wind tunnel showing nitrogen storage, vacuum tank, and flow conditioning. (b) Image of wind tunnel with test article and optical window installed.

2.3. Optical equipment

A Ti:Sapphire femtosecond laser system (Spectra Physics, Solstice:Ace) was used during this experiment to provide the FLEET excitation for velocity measurements. The laser is regeneratively amplified to

produce up to 7 mJ/pulse at a 1 kHz repetition rate with 800 nm center wavelength and 100 fs pulse duration. The femtosecond laser is located outside of the wind tunnel laboratory in a separate humidity and temperature controlled room to reduce the negative impacts of the harsh test cell environment during tunnel runs. The beam is routed towards the wind tunnel through a series of mirrors to an optical table next to the test section. On the optical table, the beam travels through a λ/4 waveplate, a periscope, a 1:2 telescope, 30:70 and 50:50 beamsplitters and ultimately three +250 mm focal length plano convex lenses before entering the test section through the front window. The waveplate is installed to allow optimization of the laser polarization for maximum performance of the beamsplitters and mirrors in the optical system. The periscope allows the beam to be brought to the correct height to enter the test section near the top surface of the experimental article. The 1:2 telescope doubles the beam diameter from 8 cm to 16 cm, which decreases the beam waist by a factor of two, as shown in equation (1) below:

$$w_0 = \frac{2\lambda F}{\pi D} \quad (1)$$

where w_0 is beam diameter at the waist, λ is laser wavelength, F is focal length of the lens in use, and D is input beam diameter. Reducing the beam waist allows delivery of the same amount of energy into a smaller volume to improve FLEET signal generation. Another benefit of the telescope is that it increases the beam area by a factor of four prior to focusing and lowers the risk of damaging the windows from laser absorption and supercontinuum generation (20), which broadens the laser wavelength and can significantly reduce the laser energy available for tagging. After the telescope, beamsplitters are used to separate the beam into three legs so that each path can be individually focused to an interrogation point. By design, the first beamsplitter reflects 30% of the beam and transmits 70% of the beam, while the second beamsplitter transmits and reflects 50% each. While actual transmission and reflection vary depending on wavelength, polarization, and incident angle, this combination provides the closest to a uniform energy distribution between each beam path. Three +250 mm focal length lenses are placed adjacent to each other with minimal separation and the laser beams were aligned into each lens such that the foci were in close proximity (1–3 mm). With beamsplitters, multiple excitation points were produced to increase the data rate of the measurements, and to evaluate the capability of measuring instantaneous spatial velocity gradients to calculate flow properties such as shear stress. To the authors' knowledge, there is very little prior work reported on multi-point FLEET tagging. To tag different points in the flow, the locations of the beamsplitters and lenses were slightly adjusted between test runs. An overview of the laser and camera setup is depicted in Figure 4.

For image acquisition, a high-speed CMOS camera (Fastcam, SA-Z) was coupled inline to an intensifier (Lambert, HiCatt). An 85 mm lens with an 8 mm extension ring and an aperture of *f*/1.4 provided the imaging system a magnification of 4.9 pixels per millimeter with a field of view of 384 pixels in the streamwise direction and 160 pixels in the vertical direction. To set the magnification of the imaging system, the spot displacement was estimated a priori based on the expected flow velocity from computational fluid dynamics (CFD) simulations. At a maximum velocity of 650 m/s and a total imaging time of 100 microseconds, a tagged spot will move 65 millimeters in the flow direction, or 318.5 pixels in the camera frame. This provides a near maximization of the relative motion of the excited spots in the camera field of view and ensures the highest precision to measure velocity. As the predicted flow is mostly axial, there is additional space in the vertical direction of the field of view of the camera so that the imaging system can investigate alternate locations in the wall-normal direction without movement and re-calibration of the camera, which would be prohibitively time-consuming. For data collection, the imaging system is framed at 200 kHz, or one image every 5 μs. In (10) it was shown that longer time delays between images can lead to higher precision, although this has the effect of spatially averaging the measured velocities. As the velocity gradients are high for supersonic flows subject to shock waves, the shortest time delay allowable by the imaging system was selected to capture the smallest spatial flow features. To save on data collection, the camera is operated in a burst mode where only 20 frames of the FLEET signal are captured per laser pulse. The intensifier gate was set to 1000 ns, and the gain was set between 800-900 volts (85-95% of maximum). To reduce spurious noise in the data at high intensifier gain, special care was taken to eliminate stray light entering the test cell during testing.

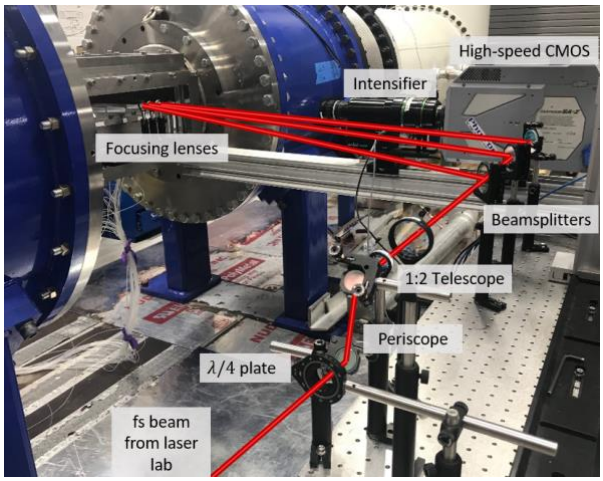

Figure 4. Laser and camera experimental setup.

3. Data processing

Various steps need to be taken to transform the raw image sequences into position and velocity measurements. These include data organization of image sequences, centroid finding, and velocity calculation. These steps are summarized in the proceeding sections.

3.1. Data organization

During data collection, the images are saved as a sequence whose length is a function of the acquisition period. During processing, these sequences are rearranged into a 4-dimensional array with the last dimension being the index of the image with respect to the laser pulse. This results in a 384×160×N×20 matrix, where the first two indices denote the number of pixels in the images, N is the number of total acquired measurements, and 20 is the number of obtained images per laser excitation. As the excited spots continue to fluoresce as they travel downstream, the 20 successive images allow additional velocity measurements along the path line of the tagged molecules. The upper limit of N, the number of sequential measurements that can be taken during one acquisition is set by the on-board memory of the camera which can hold 74,240 images and corresponds to 3712 individual measurements over a time span of 3.7 seconds. During a typical experiment, this full memory capability was not used, and the N value was 500 to foster acquisition of proper statistical measurements. This value of N necessary observations would be the same if PIV were implemented to measure the velocity field in this test article. Since multiple excitation spots are drawn in each image, the spots must be isolated with respect to one another. While automated spot finding is possible to an extent, the isolation step is performed manually. The data are collapsed into a 384×160×20 matrix of average images for each frame index. From here, a region around each spot is selected for the algorithm to begin the centroid analysis. A time series of raw data with associated isolation regions is plotted in Figure 5.

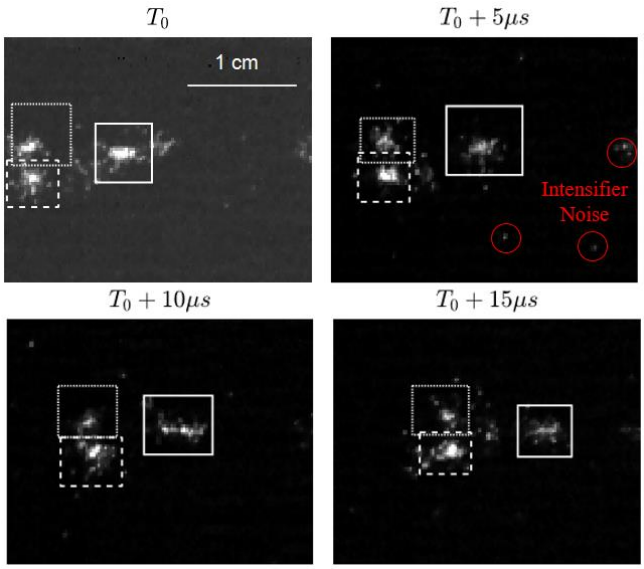

Figure 5. Time series of raw data with spot isolation regions. Spurious intensifier noise is highlighted in red, which was subtracted during image processing.

3.2. Centroid analysis

After spots are individually isolated, their absolute position must be found. Typically, either a Gaussian surface fitting (15), or cross- correlation (17,18) have been employed to analyze FLEET data. In previous works (18), it was shown that there is a negligible difference in accuracy between the cross-correlation method and the simpler weighted centroid method. In situations where cross-correlation is used for velocity, a separate step for finding the spot position must still be taken (17). The weighted centroid finding scheme was chosen for its balance between accuracy and lower computational expense. To perform the method, a cut-off intensity for all images was chosen as two times the root-mean-square background intensity value. In the following step, each pixel with an intensity above the cut-off is multiplied by its location in either the *x*- or *y*-direction and all weights are summed. This weight is divided by the total image intensity to obtain the centroid location. Equations 2 (a) and (b) outline the algorithm

for finding the *x*- and *y*- centroids of an image with this method.

$$\bar{X} = \frac{\sum_{i=1}^{columns}\sum_{j=1}^{rows} Intensity(i,j) * i}{\sum_{i=1}^{columns}\sum_{j=1}^{rows} Intensity(i,j)} \qquad (2a)$$

$$\bar{Y} = \frac{\sum_{i=1}^{columns}\sum_{j=1}^{rows} Intensity(i,j) * j}{\sum_{i=1}^{columns}\sum_{j=1}^{rows} Intensity(i,j)} \qquad (2b)$$

The cutoff intensity is a critical parameter in the centroid finding algorithm which, if not adequately selected may yield high bias in the results. Additionally, the background of the image has a non-zero intensity, which can lead to a bias in the location of the centroid if the algorithm does not take this into account. The noise in each image is comprised of two main aspects: camera chip noise and intensifier electrical noise. The camera noise can be predicted and easily eliminated, because it remains nearly constant through all frames. The electrical noise from the intensifier is slightly harder to account for, and exhibits a random behavior. Small illuminated spots of intensifier noise are circled in red in Figure 5. A cutoff intensity to account for these random noise spots is selected by applying a factor of 2 to the mean background intensity level. This centroid finding procedure is performed individually for each isolated spot in its interrogation region, and then the offset of the interrogation region to the base image is added to the centroid location to achieve the absolute position of the spot.

3.3. Velocity calculation

To perform velocity calculations after the spot locations are defined, finite differencing and spatial calibrations are applied. After optical setup and before data acquisition, a calibration image is recorded. A grid target of known size is placed into the camera field of view. At low laser energy and without operating the camera, the calibration grid is moved to the focal point of the laser beams. When in position, the laser is turned off and the camera is focused. With the lens aperture fully opened to decrease the focal depth, the camera is focused onto the target. Opening the aperture serves to increase the sensitivity of focusing to ensure the best results. Once a calibration image is acquired, the camera focus is locked and the aperture can be set appropriately for data collection.

The spatial calibration is adopted to convert the position of all spots in pixels to an absolute location in meters. First order finite differencing is used to determine the spot velocity between the $\boldsymbol{i^{th}}$ and $(\boldsymbol{i+1})^{\boldsymbol{th}}$ locations. Since the velocity measurement is path averaged between the two spots, the location of the velocity measurement is reported at the midpoint between the two locations. In previous works, higher-order finite differencing (15,17) as well as smoothing and optimal path definition (17) were demonstrated to improve the accuracy of the measurement. These methods were applied to subsonic flows where velocity was assumed to vary smoothly. From prior characterization of the wavy hub surface via experimental Schlieren and computational fluid dynamics (CFD), the existence of multiple shock interactions was proven, meaning the flow field could not be assumed to vary smoothly or continuously. For this reason, more complex velocity evaluation methods were not investigated for this work as they might smooth out the results spatially. Since FLEET measurements are non-instantaneous, there is a high effect of flow velocity and camera frame rate on the streamwise resolution of velocity measurement. In high supersonic velocity flow fields where FLEET is an attractive tagging method, the signal can move several millimeters in the time between images. Minimization of interframe time is preferred to increase the spatial resolution of measurements for this experiment.

Upon calculation of all velocities, some data points appear to be anomalous and non-physical. These points need to be reviewed manually and many are a result of the FLEET signal spatially overlapping with background reflections that were not mitigated at the time of the experiment. These outlier datapoints were then manually removed from the results.

3.4. Measurement Precision and Accuracy

In previous experiments (15–17) conducted in subsonic closed-loop facilities, measurement accuracy was evaluated with respect to reference velocities set in the wind tunnel. By performing simultaneous FLEET and probe measurements over the operating envelope of the facility, an uncertainty correlation was created. For short-duration supersonic blow down tunnels, such as the one used in this experiment, performing this comparison is not feasible. To gain an understanding of the measurement precision in this case, wind-off data

was collected. Since there is no flow in the wind tunnel, the theoretical velocity is 0 m/s. 50 datapoints were taken with FLEET and the standard deviation of the velocity measured is taken as the precision of an instantaneous measurement, which is 33 m/s. For this experiment, this correlates to an average bias shift of 0.8 pixels in the centroid location of the FLEET signal at zero flow.

This is worse than reported in previous experiments (15–18) because of the processing method and the flow conditions at which the zero data was taken. Previous researchers increased precision by averaging the velocity along several downstream spot observations, yielding a trade-off between spatial resolution and precision. This could not be performed in the current research because there are numerous shock waves along the streamlines. Prior to the test, the wind tunnel pressure is below 100 mbar; at such sub-atmospheric pressure, low number density and diffusion cause an increase in the size of the apparent FLEET spot (8). While an increase in spot size does not necessarily cause a decrease in accuracy, the diffusion and mixing of the spot due to the flow causes a changing spot shape, which adds a bias to the individual centroid locations and increases the uncertainty of the measurement. Because of FLEET signal degradation at no-flow test conditions, the actual uncertainty may be improved at flowing conditions. At a mean flow velocity of 500 m/s, the uncertainty on the instantaneous measurement corresponds to 6.6%. Further improvements to laser focusing, image acquisition and data filtering may lower this uncertainty to levels demonstrated in previous experiments. Comparable uncertainties from PIV experiments in supersonic wind tunnels can approach 2% (21); however, the validity of the results across shock waves is questionable.

The mean velocity for the zero-flow data is .3 m/s, however no other comparable data is available at high speed due to the unsteady nature of the flow field. Additionally, the accuracy of the time-averaged measurements can be inferred from two main components that make up the error: the uncertainty associated with the time between camera frames, and the uncertainty associated to the spot centroid finding. Thus, the relative velocity accuracy can be computed by Equation 3:

$$\frac{dV}{V} = \sqrt{\frac{dX^2}{X} + \frac{dt^2}{t}} \qquad (3)$$

where dV is the velocity uncertainty, and dX and dt are the uncertainties related to the distance and the time. For the camera system, the timing uncertainty is <10ns. By comparing the results of the centroid finding from the previously described weighted centroid method with a two-dimensional Gaussian surface fitting, the average disagreement in centroids is .13 pixels. Time spacing is always 5 microseconds between images, but the distance (X) the signal travels is dependent on the velocity, and results in a velocity dependent accuracy. With this uncertainty in time and distance, the accuracies at 200, 400 and 600 m/s are 2.64, 1.34, and .90 % respectively. The accuracy increases for increasing velocity, because the percent uncertainty in the centroid location decreases with increasing total displacement. A similar result is achieved and noted in (130) where an increased time delay leads to higher accuracy because the signal has traveled further.

4. Results

The most important improvement of the FLEET measurement technique is the increased spatio-temporal resolution and ability to measure highly dynamic flow structures and transient events. The method has already been shown to work well for categorizing flow fields in a time-averaged manner. By obtaining spatially resolved instantaneous velocities, additional data can be extracted from the experiment such as shear stress. With beam splitters, multiple focal points could be produced and resulted in the ability to resolve these instantaneous velocity gradients. Specifically, 4 features relevant for high-speed internal flows could be addressed with this new non-intrusive measurement technique and are described below.

4.1. Evaluation of the mean flow physics and validation for computational tools for high speeds flows

Schlieren visualization is used to illustrate the dominant flow features, as shown in Figure 6. A first compression shock compresses the flow due to the increase in amplitude of the wavy contour of the lower wall (hub). In the aft part of the wavy contour, a separation shock is formed as well as a shear layer and a subsequent recompression zone at the onset of the second wavy

contour. An unsteady shock-boundary layer interaction (SBLI) arises due to the interaction of the compression shock and the upper wall (shroud).

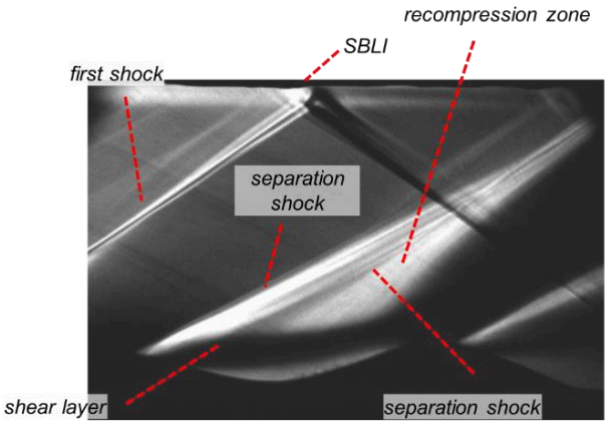

Figure 6. Flow field description via Schlieren visualization.

a. Mean and fluctuating flow field

All measurements from the steady-state tests were added together to obtain a statistical view of the flow field of the aft part of the first wavy contour and the onset of the second wave. All statistical mean values were calculated from 500 samples to ensure proper calculation of the mean. Figure 7 adds a velocity-oriented context to the flow features of Figure 6. In Figure 7(a) the average flow field vectors are visualized. The flow experiences a slight upward component as it travels over the first wavy contour due to the presence of the first compression wave (which results in an oblique shock further away from the hub boundary). At the descent of the wavy contour, the flow turns due to expansion fans up to the location of the separation shock, which turns the flow back towards the axial direction. Downstream, at the onset of the second wavy contour, the flow is again compressed with consequent positive flow angles. The overall magnitude of velocity is highest in the acceleration zone, and is slightly lower upstream and downstream of this flow feature. The level of flow unsteadiness is visualized through the fluctuation level vectors in Figure 7(b). This plot displays the standard deviation of velocity over the set of all measurements at each location. The mean axial flow component for all points is generally steady, proven by the rather vertical nature of each vector. Upstream of the separation shock the flow experiences small fluctuation vectors, with standard deviations ~20 m/s, within the experimental uncertainty. Proceeding into the acceleration zone, the fluctuation magnitude grows due to the presence of the unsteady separation shock. In most downstream measurements, the fluctuation levels decrease again due to the absence of unsteady shock patterns. The highest levels of fluctuation, however, can be observed in the measurements nearest to the surface. At this location, velocity is influenced by the shear layer created by the separation region of the first wavy contour.

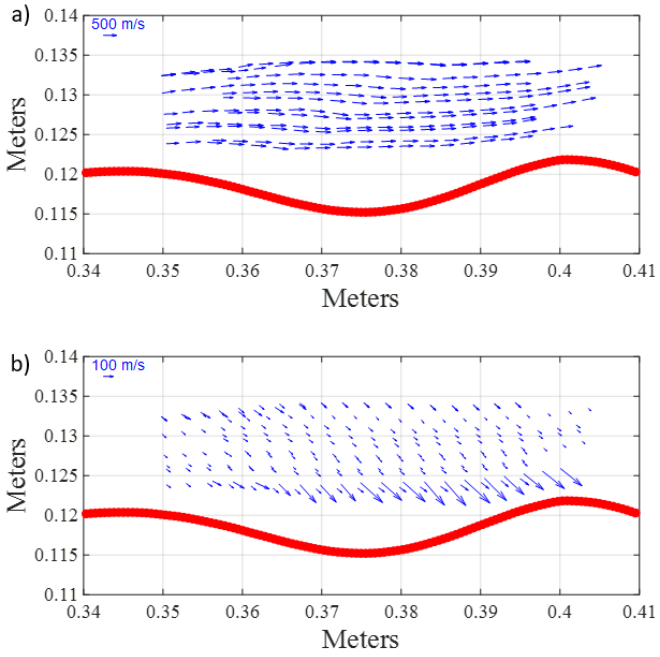

Figure 7. (a) Average velocity vectors obtained from all FLEET measurements. (b) Fluctuation level (standard deviation) vectors for all measurements.

b. Flow field comparison to CFD

In between test runs the laser foci were traversed through the measurement region to tag different locations in the flow field, which enabled a statistical interrogation of the flow structures. CFD simulations were performed for benchmark comparison and to obtain insight in the regions with important flow field features that need to be captured with the FLEET measurement technique. For these simulations, The Reynolds Averaged Navier-Stokes (RANS) equations were solved with Metacomp from CFD++, a commercial computational fluid dynamics (CFD) software package (22). The turbulence closure was provided by the k-omega shear stress transport (SST) model. The non-dimensional wall distance was kept below one to solve the viscous sublayer and the entire converging-diverging nozzle was

modelled. Further details about the simulations can be found in (23). Figure 8 shows a comparison of the CFD simulated axial velocity component to the measured velocity in the experiment. The FLEET measurements are overlaid on the CFD contour in (a) and plotted on the same colormap. This gives an initial indication of the agreement between the two values. The percent error between the two is given by the points in (b).

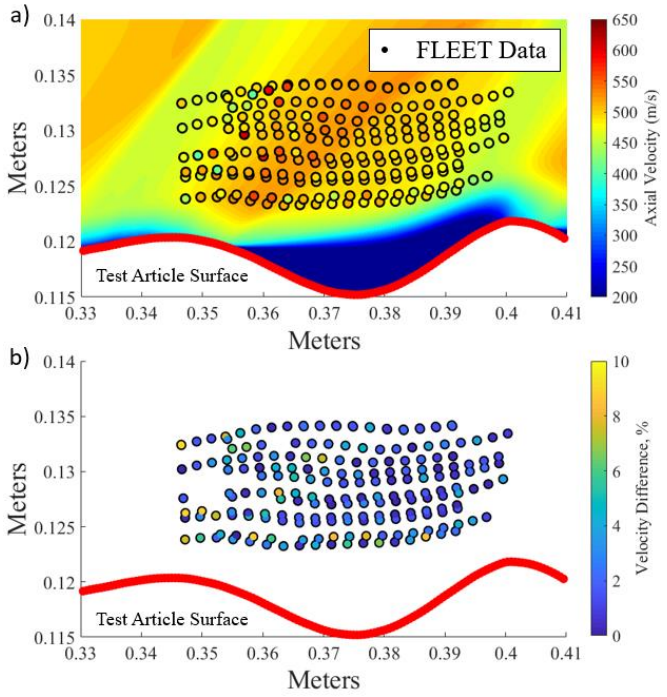

Figure 8(a) Overlay of CFD predicted axial velocity and FLEET measurements, (b) Percent difference between FLEET and CFD at each measurement point.

The average difference between the measurements and CFD is 2.2%. The larger values of disagreement appear near where the separation shock appears above the shear layer and near the bottom of the flow field where the separation region is beginning.

Figure 9 (a) shows the CFD contour of transverse velocity, and (b) displays the same contour made from the FLEET measurements. To create the contour for (b), the data was interpolated and extrapolated from the discrete datapoint locations shown in Figures 7 and 8 to create a continuous profile. The bounds for the extrapolation were set to the x- and y-extrema of the datapoint locations. Qualitatively, the simulation agrees well with the measurements. The separation shock is clearly captured by the FLEET measurements as well as the recompression zone downstream, in which the flow turns to positive transverse velocities. In (b) a number of non-uniformities in the contour are observed which are due to the sparsity of FLEET data points used in this experiment. To gain a more uniformly converged flow field contour, more data points with a calibrated traverse system can be implemented.

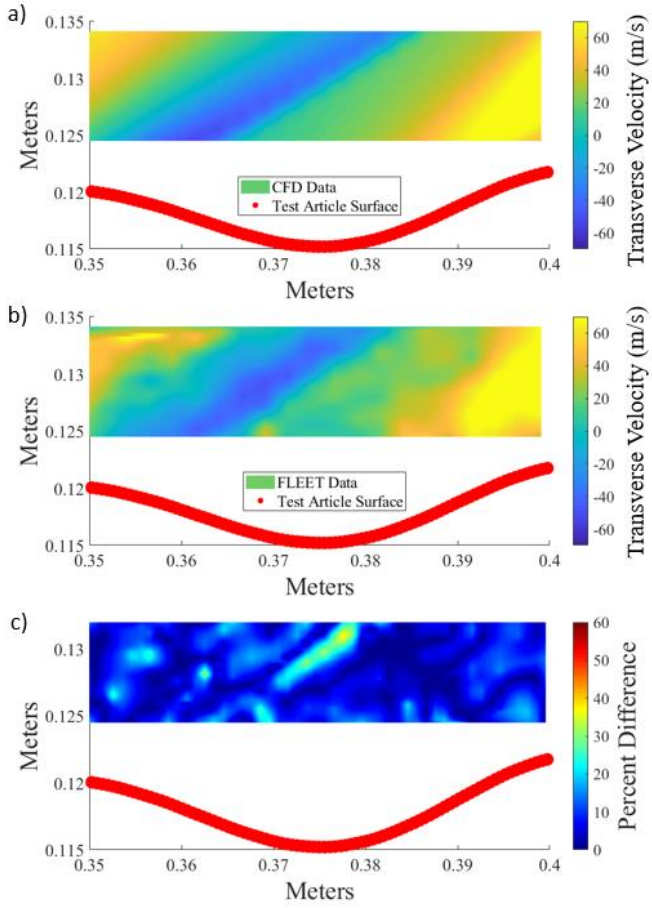

Figure 9 (a) CFD predicted transverse velocity, (b) interpolated transverse velocity from FLEET measurements, (c) percent difference between CFD and FLEET velocities

The difference between the contours in (a) and (b) is depicted in Figure 9 (c), and this further displays the disagreement between CFD and FLEET. Many locations in the contour exceed 10% disagreement, and this is more pronounced because the transverse flow component is an order of magnitude smaller than the axial flow component. Again, localized smaller spikes in disagreement can be attributed to sparsity in the data point locations. However, a clear region of up to 40% disagreement is visualized, which reflects the location of the separation shock.

Figures 8 and 9 reveal that the RANS simulations locally mis-predict the vicinity of the separation shock and the region of the shear layer compared to FLEET. This is due to the inability of

RANS to properly capture the separation point (24), leading to misprediction of the aero-thermal properties at these locations.

4.2. Measurement of the unsteady flow fluctuations

Shock-boundary layer interactions inherently cause unsteadiness. To evaluate flow unsteadiness, probability density functions (PDFs) are calculated and Figure 10 depicts the PDFs of six select points in the flow. The points of interest are shown on the CFD contour in (a) and are color-coded to their respective PDF in (b). Normalized PDF's with respect to the mean velocity magnitudes are displayed in (c).

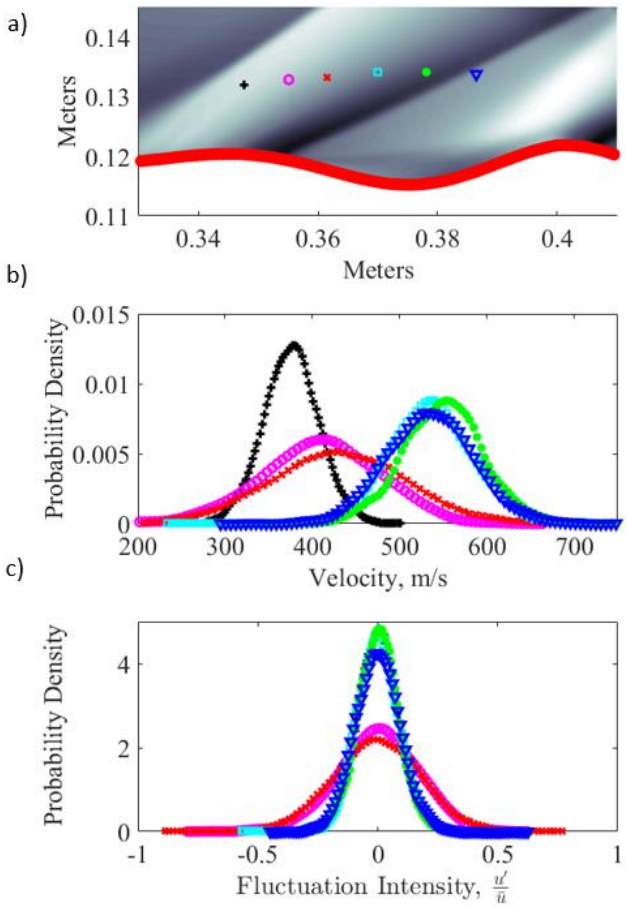

Figure 10 Probability density functions at (a) select points in the flow of (b) velocity and (c) fluctuation intensity from FLEET measurements.

The black (+) point has a concentrated probability density function. This shows that the velocity at this point is relatively steady with velocity fluctuations indicated by a standard deviation of ±15%. The magenta (o) and red (x) points have similar distributions to one another. This part of the flow lies in the region upstream of the strong acceleration region and at the same axial location of the separation shock, which could explain for the high local unsteadiness. The standard deviation of the fluctuations is around ±25% for these points. The cyan (□) and green (•) points have somewhat broad PDFs featuring less unsteadiness than the previous points and lie in the acceleration region upstream of the separation shock, whereas the blue (▼) point lies just downstream of the separation shock. The unsteadiness in the latter region is additionally influenced by the shear layer downstream of the first wavy contour and the consequent interaction with the recompression wave.

4.3. Unsteady flow shear stress measurement

By aligning two or more FLEET focal volumes in close proximity, instantaneous measurements of shear stress could be extracted.

To calculate shear stress, the following equations were solved:

$$\tau = \mu \frac{du}{dy} \qquad (4a)$$

$$\frac{T_0}{T_s} = 1 + \frac{\gamma - 1}{2} M^2 \qquad (4b)$$

$$M = \frac{U}{\sqrt{\gamma R T_s}} \qquad (4c)$$

$$\mu = \mu_0 \left(\frac{T_s}{T_0}\right)^n \qquad (4d)$$

Parameters $\mu_0 = 1.782 * 10^{-6}$ Pascal seconds, $\gamma = 1.4$, and $R = 296 \frac{J}{Kg\ K}$ are assumed for nitrogen. $T_0 = 270$ Kelvin and is known from the facility operating point. U and $\frac{du}{dy}$ are known from the FLEET measurement results. The remaining parameters including the shear stress, τ, are calculated for each velocity measurement via equations 4(a-d). The velocity difference between two points had nominal separation of

3 mm and the corresponding shear stress are shown in Figure 11.

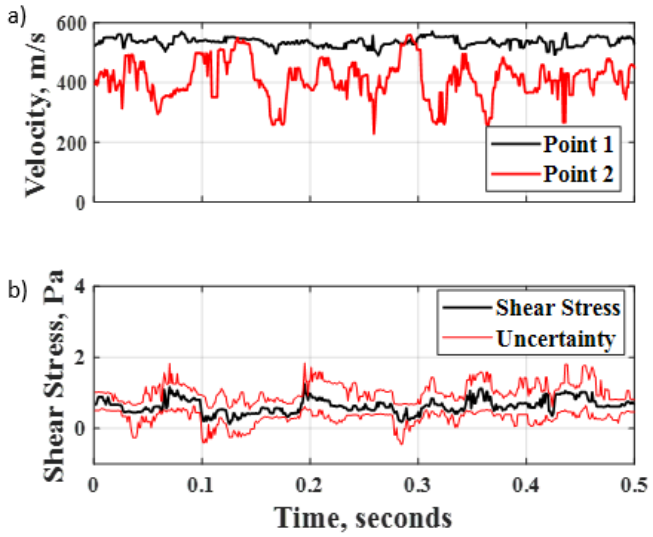

Figure 11 a) Velocity of two measurement points tagged simultaneously. (b) Shear stress between points as a function of time.

The measured shear stress fluctuates around .68 pa, with a standard deviation of 1.38 Pa due to large fluctuations in the velocity at point 2. Uncertainty in the shear stress value is calculated by propagating the velocity uncertainty through the calculation of shear stress to give upper and lower bounds for each value. Multi-point FLEET tagging can thus be used to measure instantaneous flow shear.

4.4. Measurement of highly transient spatial occurrences: unstarting

During start up and shutdown of the supersonic turbine, a transient normal shock wave advances along the turbine passage creating a localized increase in static pressure and temperature, which is capable of causing a catastrophic event. At the beginning of the test, the transition from no-flow, subsonic towards supersonic velocities, requires this normal shock wave to move downstream of the turbine passage. By contrast, during the shut-down process, the normal shock wave travels upstream, and the flow decelerates to subsonic conditions. This process is known as unstarting. The time-dynamics of this phenomenon have critical relevance to any supersonic passage flow. The accurate characterization of this phenomenon is required to design adequate internal passages exposed to transient operation, such as in supersonic turbomachinery or supersonic intakes. The entire process is highly dependent on the status of the boundary layer, and therefore conventional CFD may cause mispredictions, so experimental data is required to improve our models. Unstarting could be achieved by a sudden decay of the upstream pressure (closure of the upstream valve), or a gradual increase of the back pressure caused by the filling up of the downstream vacuum tank. FLEET was used to capture the first transient event and to track the spatio-temporal evolution on the flow field. A shadowgraph sequence of the shutdown of the turbine passage is displayed in Figure 12 **Error! Reference source not found.**(a-e). Due to the elevated back pressure at the end of the test, the rear part of the test section was already ‘unstarted’ (no separation shock is detected near the second wavy contour). When the valve is closed, a shock wave travels upstream followed by a zone of supersonic/subsonic flow until the flow becomes subsonic and ultimately decreases to zero velocity. Total time to ‘unstart’ for this experiment is around 250 ms, and the limitation is set by (1) the closing of the upstream valve, which was ~100 ms, and (2) the pressure ratio. Additionally, during shut down, shock waves seem to be locally moving back and forth on top of the shear layer.

Figure 12 (a-e) illustrates the entire sequence conducive to the unstarting of the supersonic passage. At the onset of unstarting numerous shocks are formed, the elevation of back pressure causes the separation region to enlarge and become more unstable. Several velocity locations are plotted in Figure 12 (f). A median filter with a 21 sample wide window is applied to smooth out random fluctuations. An initial deceleration from 0.5–0.6 s is seen in all interrogated points due to the onset of unstarting, as also highlighted in the shadowgraphs of Figure 12 a). At time 0.6 s in (Fig 13b), the first separation shock already lifts off and moves upstream. Between these two time steps the velocities of all interrogated points have dropped drastically due to altering flow field. Point 3, in blue, shows a small increase in velocity between 0.6 s and 0.65 s, caused by the instantaneous acceleration in the free stream. From (b) and (c) a grouping of reflected oblique shocks anchored on the shear layer in the aft part of the first wavy contour is observed. This pattern persists for a few tens of milliseconds, and the velocities at points 4 and 5 remain steady during this time. Between 0.65 s and 0.75 s in (c–e), the velocity at point 3 drops drastically while points 4 and 5 remain constant. Points 16 and 17 continue decreasing at a moderate rate due to the increasing back pressure. After the passing of the

terminating shock at 0.7 s, lambda-shock structures appear, and the entire flow field becomes subsonic. In (e) one of these waves is seen right at the location of Points 16 and 17. Soon after the moment that the pressure wave passes upstream of these points, their velocities drop significantly. Shortly after, points 4 and 5 experience the same phenomenon. After the upstream propagation of these waves, the pressure is equalized over the entire field and the flow speed in the test section drops to zero. This measurement shows the ability of FLEET to capture the time-evolution of a spatially resolved transient event. Previous works have described the application of FLEET to transient wind tunnel startup (25) measurements, however the results were limited to one point and were taken in the freestream of the wind tunnel. This work provides an improvement by quantifying time-resolved description of shock structures over a turbine-relevant test article.

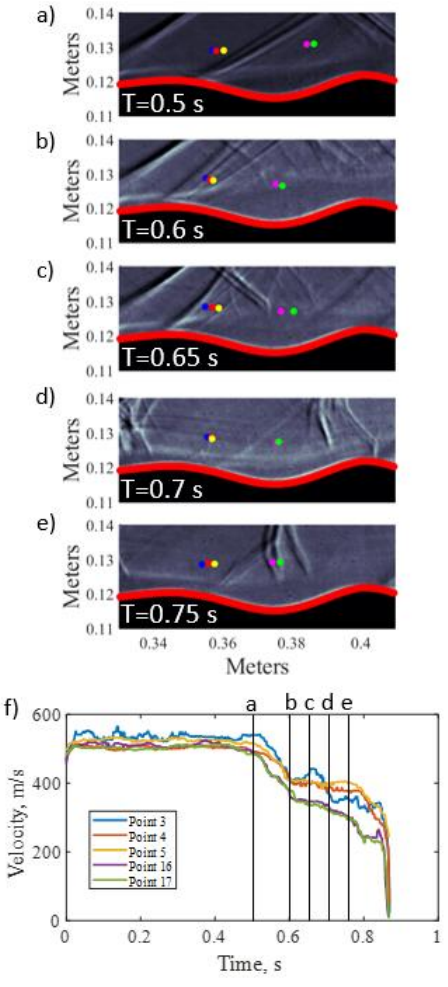

Figure 12. (a-e) instantaneous shadowgraph images during unstarting of the test section. (f) Velocity trace of color-coded points in the unstarting flow field from FLEET measurements.

5. Conclusions

Femtosecond Laser Electronic Excitation Tagging (FLEET) was used to optically evaluate the complex supersonic flow over a wavy hub surface representing two-dimensional model of a bladeless turbine. The molecular nitrogen tracking employed in this experiment allowed measurements within the high gradients of velocity caused by compression and separation shocks. Uncertainties were found to be around 6.6% for a mean flow velocity of 500 m/s. Measurements of velocity components compared well to CFD simulations, but disagreed in the precise location of the separation shock. Probability density functions were adopted to evaluate the unsteadiness at different locations, which are caused because of multiple shocks, shock boundary layer interactions, and shock-shear layer interactions. Demonstration of instantaneous shear stress measurements with multi-point FLEET tagging were shown. Finally, the transient flow phenomena that occur during shut down of the turbine were quantified and overlaid with shadowgraph results.

Acknowledgements

The authors thank the PETAL research team for their aid during the preparation and execution of the experiments. The authors also acknowledge Scott Meyer for his leadership to set up the nitrogen high pressure system, and Mikhail Slipchenko for assistance developing optical arrangements.

ORCID iDs

J Fisher https://orcid.org/0000-0001-6834-0181
J Braun https://orcid.org/0000-0003-4774-4456
T Meyer https://orcid.org/0000-0002-2071-142X
G Paniagua https://orcid.org/0000-0002-2437-4045

References

[1] Vinha N, Paniagua G, Sousa J, Saracoglu B H, "*Axial fluid machine and method for power extraction,"* European Patent EP 2868864 A1, May 2015.
[2] Braun J, Paniagua G , Falempin F, Le Naour F, "*Design and Experimental Assessment of Bladeless Turbines for Axial Inlet Supersonic Flows*", Proceedings of the ASME Turbo Expo, June 2019, GT2019-91047, Phoenix, AZ
[3] Tedeschi G, H. Gouin H, Elena M, "*Motion of Tracer Particles in Supersonic Flows*", Experiments in Fluids (1999) 26: 288. https://doi.org/10.1007/s003480050291.

[4] Thomas P J, *"On the influence of the Basset history force on the motion of a particle through a fluid,"* Physics of Fluids A: Fluid Dynamics **4**: 2090 (1992); https://doi.org/10.1063/1.858379.

[5] Boiko V M, Zapryagaev V I, Pivovarov A, Poplavski S V, *"Correction of PIV data for reconstruction of the gas velocity in a supersonic underexpanded jet,"* Combustion, Explosions, and Shock Waves (2015) 51: 587. https://doi.org/10.1134/S001050821505010X.

[6] Petrosky B J, Lowe K T, Bardet P M, Tiemsin P I, Wohl C J, Danehy P M, and Andre M, "*Particle Image Velocimetry Applications Using Fluorescent Dye-doped Particles*", AIAA Paper 2015-1223, 53rd AIAA Aerospace Sciences Meeting. Kissimmee, Florida, 5-9 January 2015.

[7] Michael J B, Edwards M R, Dogariu A, and Miles R B, "*Femtosecond laser electronic excitation tagging for quantitative velocity imaging in air*," Applied Optics 50, 5158-5162 (2011).

[8] DeLuca N J, Miles R B, Kulatilaka W D, Jiang N, and Gord J R. "*Femtosecond Laser Electronic Excitation Tagging (FLEET) Fundamental Pulse Energy and Spectral Response*", 30th AIAA Aerodynamic Measurement Technology and Ground Testing Conference, AIAA AVIATION Forum, (AIAA 2014-2227), https://doi.org/10.2514/6.2014-2227

[9] Danehy P M, Bathel B F, Calvert N D, Dogariu A , and Miles R B. "*Three Component Velocity and Acceleration Measurement Using FLEET*", 30th AIAA Aerodynamic Measurement Technology and Ground Testing Conference, AIAA AVIATION Forum, (AIAA 2014-2228), https://doi.org/10.2514/6.2014-2228.

[10] Peters C J, Danehy P M, Bathel B F,Jiang N, Calvert N D, and Miles R B, "*Precision of FLEET Velocimetry using High-Speed CMOS Camera Systems"* 31st AIAA Aerodynamic Measurement Technology and Ground Testing Conference, AIAA AVIATION Forum, (AIAA 2015-2565), https://doi.org/10.2514/6.2015-2565

[11] Danehy P M, O' Byrne S, Frank A, Houwing P, Fox J S, and Smith D R, *"Flow-Tagging Velocimetry for Hypersonic Flows Using Fluorescence of Nitric Oxide",* AIAA Journal 2003 41:2, 263-271, https://doi.org/10.2514/2.1939.

[12] Sánchez-González R, Srinivasan R, Bowersox R D W, North S W, *"Simultaneous velocity and temperature measurements in gaseous flow fields using the VENOM technique"*, Optics letters. 36. 196-8. https://doi.org/10.1364/OL.36.000196.

[13] Miles R B, Cohen C, Connors J, Howard P, Huang S, Markovitz E, and Russell G, "*Velocity measurements by vibrational tagging and fluorescent probing of oxygen*," Optics Letters 12, 861-863 (1987). https://doi.org/10.1364/OL.12.000861.

[14] Forkey J N, Finkelstein N D, Lempert W R, and Miles R B. "*Demonstration and characterization of filtered Rayleigh scattering for planar velocity measurements*", AIAA Journal 34:3, 442-448 (1996). https://doi.org/10.2514/3.13087

[15] Burns R A, Danehy P M, Jones S B, Halls B R, and Jiang N. "*Application of FLEET Velocimetry in the NASA Langley 0.3-Meter Transonic Cryogenic Tunnel*", 31st AIAA Aerodynamic Measurement Technology and Ground Testing Conference, AIAA AVIATION Forum, (AIAA 2015-2566), https://doi.org/10.2514/6.2015-2566

[16] Burns R A, Peters C J, Danehy P M, "*Unseeded velocimetry in nitrogen for high-pressure, cryogenic wind tunnels: part I. Femtosecond-laser tagging*" Measurement Science and Technology 29 115302, (2018), https://doi.org/10.1088/1361-6501.

[17] Burns R A and Danehy P M, "*FLEET Velocimetry Measurements on a Transonic Airfoil*", AIAA Paper 2017-0026, 55th AIAA Aerospace Sciences Meeting, Grapevine, Texas, 9-13 January, 2017, https://doi.org/10.2514/6.2017-0026.

[18] Fisher J M, Smyser M E, Meyer T R, Slipchenko M R, Caswell A W, Gord J R, Roy S, "*Burst-Mode 100 kHz- 1 1MHz FLEET Velocimetry in Supersonic and Hypersonic Flows*," *AIAA Scitech 2019 Forum,* San Diego California, 7-11 January, 2019.

[19] Paniagua G, Gonzalez Cuadrado D, Saavedra J, Andreoli V, Meyer T R, Solano J P, Herrero R, Meyer S E, Lawrence D, 2018, "*Design of the Purdue Experimental Turbine Aerothermal Laboratory for optical and surface aero-thermal measurements*". Journal of Engineering for Gas Turbines and Power. DOI: 10.1115/1.4040683. ISSN: 0742-4795.

[20] Paschotta R, article on 'supercontinuum generation' in the *Encyclopedia of Laser Physics and Technology*, 1. edition October 2008, Wiley-VCH, ISBN 978-3-527-40828-3

[21] Beresh S J, Henfling J F, Spillers R W, Spitzer S M, "*'Postage-stamp PIV': small velocity fields at 400 kHz for turbulence spectra measurements*", Measurement Science and Technology, 29 034011, (2018), https://doi.ord/10.1088/1361-6501/aa9f79.

[22] Chakravarthy, S., Peroomian, O., Goldberg, U., and Palaniswamy, S., 1998, "*The CFD++ Computational Fluid Dynamic Software Suite*," AIAA and SAE, World Aviation Conference, Anaheim, CA. DOI: https://doi.org/10.2514/6.1998-5564

[23] Braun, J., Paniagua, G., Falempin, F., and Le Naour, B. (October 1, 2019). "*Design and Experimental Assessment of Bladeless Turbines for Axial Inlet Supersonic Flows*." ASME. J. Eng. Gas Turbines Power. doi: https://doi.org/10.1115/1.4045359

[24] Saavedra, J and Paniagua G, "*Transient Performance of Separated Flow: Experimental Characterization of Flow Detachment Dynamics*" Proceedings of the ASME Turbo Expo 2019. Phoenix, Arizona, USA. June 17–21, 2019. V006T05A016. ASME. https://doi.org/10.1115/GT2019-91020

[25] Dogariu L E, Dogariu A, Miles RB, Smith M S, and Marinneau E C, *"Non-intrusive Hypersonic Freestream and Turbulent Boundary-Layer Velocity Measurements in AEDC Tunnel 9 using FLEET,"* 56th AIAA Aerospace Sciences Meeting, 8-12 January 2018 , Kissimee, FL, https://doi.org/10.2514/6.2018-1769